Supporting Information

Bio-inspired Surface Modification of MoS_2 Nanosheets with Gallium Phthalocyanine for Brain-like Synaptic Memristor

Qizhi Jiang[1], Bin Zhang[1*], Qing Yan[1], Fei Fan[2,3], Gang Liu[2*], and Yu Chen[1*]

[1]Key Laboratory for Advanced Materials and Joint International Research Laboratory of Precision Chemistry and Molecular Engineering, School of Chemistry and Molecular Engineering, East China University of Science and Technology, Shanghai, China. E-mail: zhangbin@ecust.edu.cn; yuchenavh@ecust.edu.cn

[2]School of Electronic Information and Electrical Engineering, Shanghai Jiao Tong University, Shanghai, China. E-mail: gang.liu@sjtu.edu.cn

[3]Shanghai i-Reader Biotech Co., Ltd. Shanghai, China

Experimental section

Measurements and Instrument

All of the chemicals used in this study were of reagent grade, were purchased from Aldrich and used without further purification. Organic solvents were purified, dried, and distilled under dry argon (Ar). Few-layer MoS_2 NSs and MoS_2-PDA were synthesized according to the literature [1]. Chlorogallium(iii) 2,(3)-tetra-(*tert*-butyl) phthalocyanine (tBu$_4$PcGaCl) was synthesized according to the literature [2].

The ultraviolet visible (UV-Vis) absorption spectra were recorded using a Shimadzu UV-2600 spectrophotometer (Shimadzu, Japan). A HORIBA JOBIN YVON Fluoromax-4 spectrofluorometer (HORIBA Scientific, France) was used to record the steady-state fluorescence spectra. Fourier transform infrared (FTIR) spectra were performed wtih a Nicolet

Nagma-IR 550 spectrophotometer (Nicolet, UK) using KBr pellets. Raman spectra were recorded using a LabRAM HR Evolution Raman spectrometer (HORIBA Scientific, France) with an excitation laser at a wavelength of 532 nm. Transmission electron microscopy (TEM) images were recorded using a JEOL-2100 (JEOL Ltd., Japan) TEM system operated at 200 kV. Atomic force microscopy (AFM) images were recorded using a Dimension Icon & FastScan Bio, Nanonavi E-Sweep instrument (SII). X-ray photoelectron spectroscopy (XPS) measurements were carried out using a Kratos AXIS HSi spectrometer with a monochromatized Al KR X-ray source (1486.6 eV photons) at a constant dwell time of 100 ms and a pass energy of 40 eV. Field emission scanning electron microscope (FESEM) images and Energy dispersive X-ray spectra were recorded using a Gemini SEM 500 instrument. The electrical characteristics of the materials were investigated using a Keithley 4200A apparatus.

Synthesis of MoS_2-PDA-*t*Bu_4PcGaCl

A mixture of *t*Bu_4PcGaCl (200 mg) and MoS_2-PDA (50 mg) in anhydrous $CHCl_3$ (50 mL) was bubbled with dry argon for 30 min and then refluxed for 48 h. After cooling to room temperature, the reaction solution was dialyzed (molecular weight cut-off 1.0 kDa) against anhydrous $CHCl_3$ for 2 d. Used $CHCl_3$ was replaced with fresh $CHCl_3$ every 4 h, and then dialysis was continued against deionized water for an additional 2 d. The used water was replaced with fresh deionized water every 4 h. The collected solid product was freeze-dried for 24 h to give MoS_2-PDA-*t*Bu_4PcGaCl as a dark powder (100 mg).

Device fabrication

The ITO glass substrate (1 cm x 1 cm) was carefully pre-cleaned sequentially with ethanol, acetone, and 2-propanol in an ultrasonic bath for 15 min and then treated with oxygen plasma.

A sample solution (50 μL, 10 mg·mL^{-1}) in DMF was spin-coated on the pre-cleaned ITO sheet at a spinning speed of 800 rpm for 20 s and then at 2000 rpm for 60 s, followed by solvent removal under vacuum at 80 ℃ overnight. Al top electrodes were deposited on the surface of the active layer through a shadow mask at 10^{-7} Torr via magnetron sputtering. All electrical measurements were performed using a Keithley 4200A semiconductor parameter analyzer at ambient conditions without device encapsulation.

E_{HOMO} and E_{LUMO} of MoS_2-PDA-*t*Bu_4PcGaCl

MoS_2-PDA-*t*Bu_4PcGaCl exhibited redox behavior with an initial oxidation potential of 0.715 V and an initial reduction potential of -0.812 V, according to equations (1) and (2):

$$E_{HOMO/LUMO} = -\left[E_{onset(Ox./Red.\ vs.Ag/AgCl)} - E_{OX(ferrocene)}\right] - 4.8 \#(1)$$

$$E_g = E_{LUMO} - E_{HUMO} \#(2)$$

where $E_{\text{onset (Ox./Red. Vs. Ag/AgCl)}}$ is the initial oxidation potential and initial reduction potential of MoS_2-PDA-*t*Bu_4PcGaCl, which were 0.715 V and -0.812 V, respectively. $E_{\text{Ox(Ferrocene)}}$ is the initial oxidation potential of ferrocene, 0.39 V vs. Ag/AgCl. The highest occupied molecular orbital (HOMO) and lowest unoccupied molecular orbital (LUMO) of MoS_2-PDA-*t*Bu_4PcGaCl were calculated to be -5.125 eV and -3.598 eV, respectively, and the band gap E_g was 1.527 eV.

Supplementary Text

The solubility of MoS_2 NSs, MoS_2 -PDA and MoS_2-PDA-*t*Bu_4PcGaCl

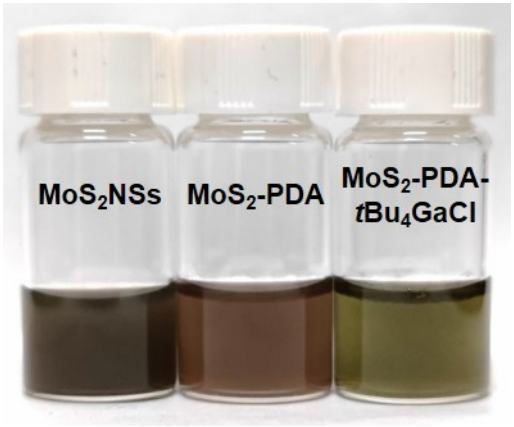

Fig. S1 The digital images of MoS_2 NSs, MoS_2 -PDA and MoS_2-PDA-*t*Bu_4PcGaCl dispersed in N,N-dimethylformamide.

The comparison of TEM and AEM images of MoS_2 and MoS_2-PDA

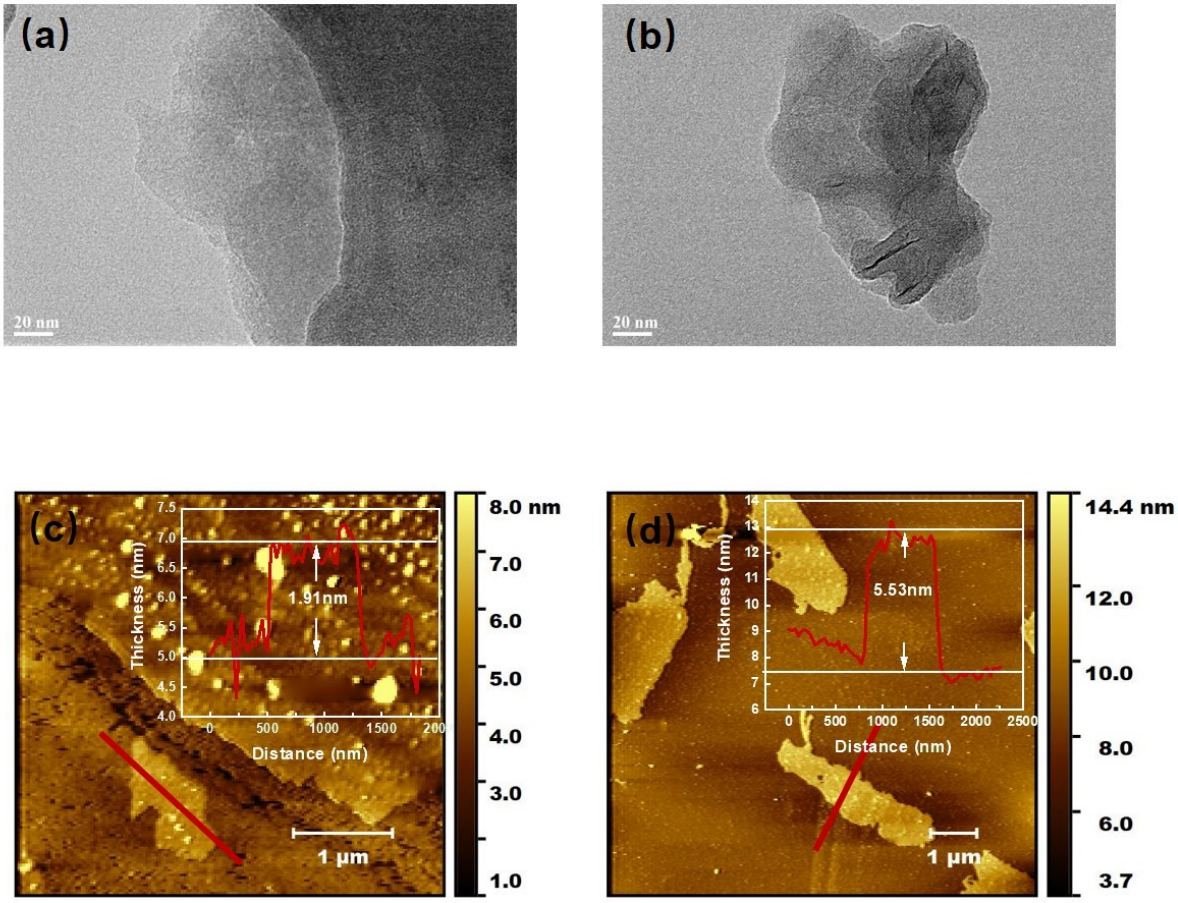

Fig. S2 TEM and AFM images of (a), (c) few-layered MoS_2 NSs; (b), (d) MoS_2-PDA.

To obtain more information about the MoS_2-PDA-*t*Bu_4PcGaCl nanocomposite components, we utilized EDX to analyze the C, O, S, N, Mo, and Ga atoms to obtain their content and distribution. **Fig. S3a** shows that the MoS_2-PDA-*t*Bu_4PcGaCl nanocomposite contained C, O, S, N, Mo, and Ga elements, in which Ga was uniformly distributed on the surface of the nanocomposite. **Fig. S3b** shows that the mass fraction of Ga element was 5.14%, which indicates that the gallium phthalocyanine content in the detected nanocomposite was about 59.5% ($W_{Ga}/W_{Ga/Pc}$, W_{Ga} = 5.14%, $W_{Ga/Pc}$= M_{Ga}/M_{Pc}= 69.4 g/mol / 806.7 g/mol = 8.64%). These results indicated that *t*Bu_4PcGaCl was successfully grafted onto the surface of MoS_2-PDA.

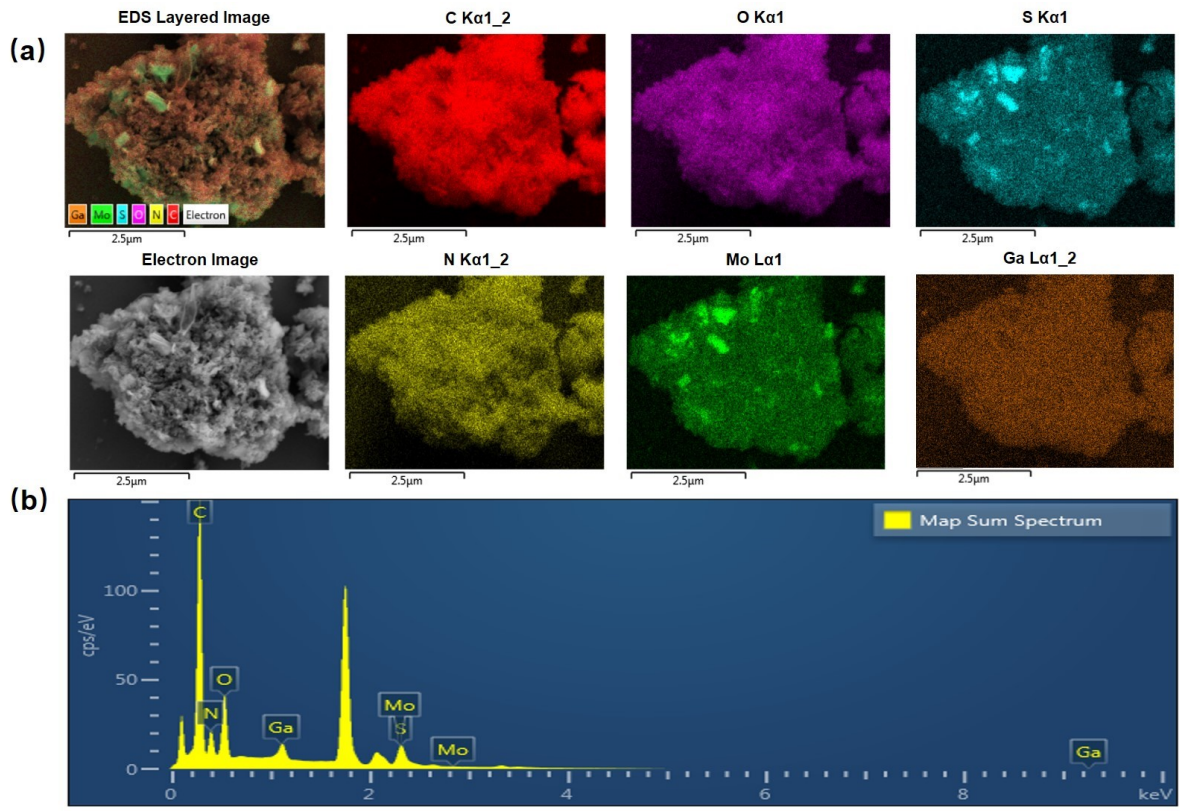

Fig. S3 (a) FESEM image of MoS_2-PDA-*t*Bu_4PcGaCl, element distribution maps of MoS_2-PDA-*t*Bu_4PcGaCl, and an overlap of the distribution maps with the FESEM image; (d) FESEM-EDS image of MoS_2-PDA-*t*Bu_4PcGaCl.

Device structure and resistive switching characteristics

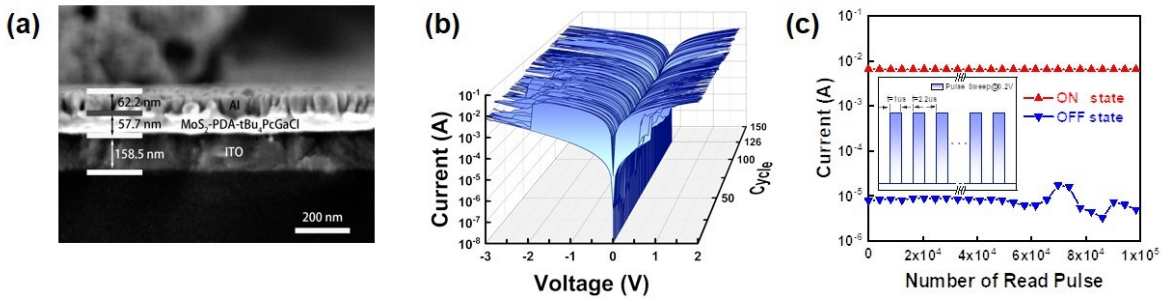

Fig. S4 (a) Cross-section SEM image of the device; (b) 3D waterfall *I*−*V* curves for 126 cycles; (c) Tolerance of the device by applying 10^5 pulses voltage (0.2 V amplitude, 1 μs pulse width, and 1.2 μs interval).

To further study the uniformity of the devices, we randomly selected 96 *I*-*V* cycle curves of 24 devices (**Fig. S6**). Devices were selected in each row and column, and four devices were

grouped as shown in the red circle for a total of six groups (**Fig. S5**).

Fig. S5 Digital photo of electronic device cells.

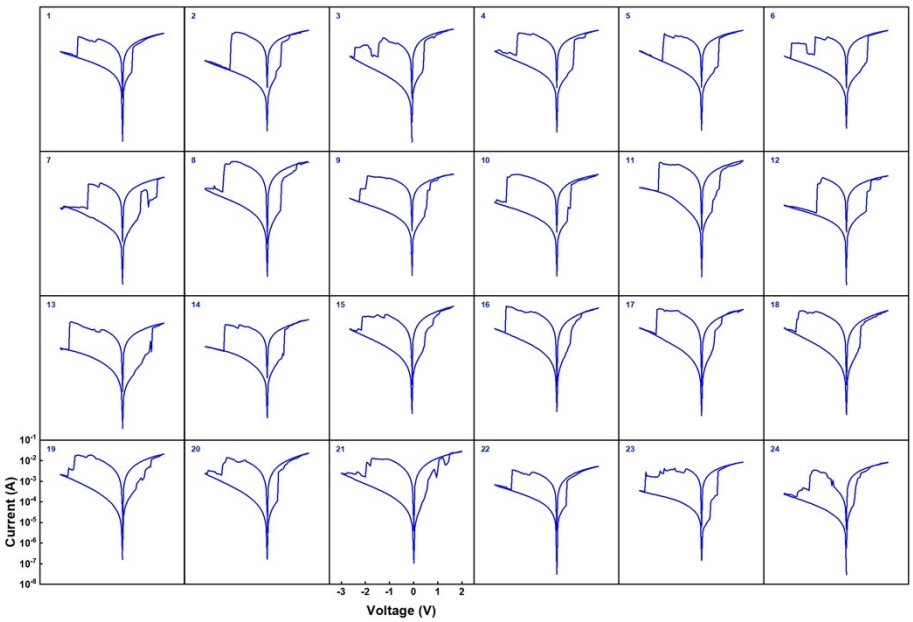

Fig. S6 *I-V* curves of 24 device cells randomly tested.

Here, we simulated the behavior of biological synapses such as PPF, PPD, SRDP, STDP, and SVDP, respectively. As shown in **Fig. S7**, the synaptic plasticity of PPF/PPD was simulated successfully. The paired-pulse positive voltage (amplitude 2.0 V, pulse width 30 μs) was

utilized for stimulation, and the pulse time interval (Δt) was gradually increased from 10 μs to 100 μs (step length = 10 μs) to explore changes in promoting the device synaptic plasticity. Similarly, the paired-pulse negative pulse (amplitude -3.0 V, pulse width 30 μs) was utilized to simulate the synaptic function of paired-pulse depression. The weights of PPF and PPD were calculated using the following equation:

$$PPF(PPD) = \frac{I_2 - I_1}{I_1} \text{x} 100\% \#(3)$$

where I_2 = the second pulse current, and I_1 = the first pulse current. According to equation (3), the scatter plot was calculated and fitted. The fitting effect of the double logarithm function was good, and its formula is as follows[3]:

$$PPF = C_1 \exp\left(-\frac{\Delta t}{\tau_1}\right) + C_2 \exp\left(-\frac{\Delta t}{\tau_2}\right) + A_1 \#(4)$$

$$PPD = C_3[1 - \exp\left(-\frac{\Delta t}{\tau_3}\right)] + C_4[1 - \exp\left(-\frac{\Delta t}{\tau_4}\right)] + A_2 \#(5)$$

where τ_1 =9.39 μs, and τ_2 = 2.86×10^6 μs are the fast and slow-decaying terms of PPF. Similarly, τ_3 = 6.24 μs and τ_4 = 1.05×10^2 μs are the fast and slow-decaying terms of PPD. Our device exhibited excellent PPF/PPD behavior and complied with short-term synaptic plasticity.

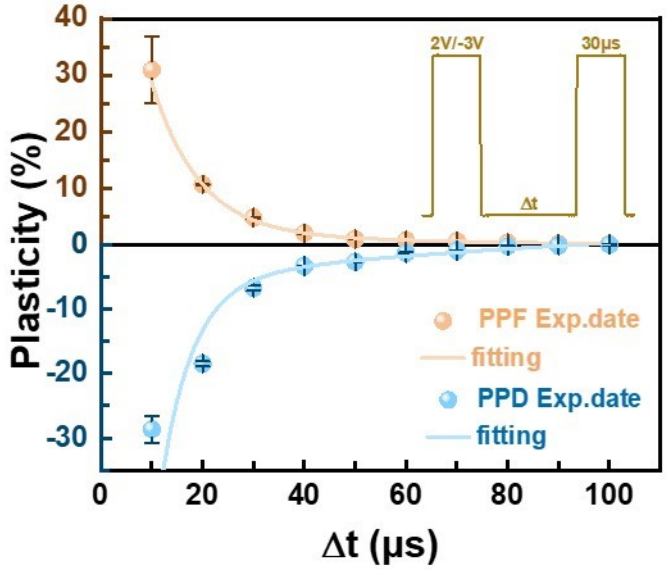

Fig. S7 Paired-pulse facilitation (PPF) and paired-pulse depression (PPD) index change with the time interval (Δt) of the double-input presynaptic pulses (2 V and -3 V respectively, 10 μs).

The successful simulation of PPF and PPD proved that our device had excellent short-term synaptic plasticity, which was manifested by the significant change in its plasticity in a short time interval and an exponential decrease upon increasing the interval time. This is exactly like PPF and PPD behavior in biological synapses. On this basis, variations in the plasticity at different rates were studied, as shown in **Fig. S9a**. The device exhibited the biological synaptic characteristics of SRDP. Under the stimulation of ten consecutive pulses with a positive voltage, different plasticity changes were obtained by varying the interval time (Δt) between adjacent pulses (amplitude 1 V, pulse width 30 μs, Δt = 10 μs, 20 μs, 40 μs, 60 μs, 100 μs). **Fig. S8** shows the pulse variation diagram. Similarly, we successfully simulated the function of negative SRDP using ten consecutive pulses with a negative pulse (amplitude -3 V, pulse width 30 μs, Δt =10 μs, 20 μs, 30 μs, 70 μs, 100 μs). Each point in **Fig. S9b** represents the pulse

current determined according to the formula:

$$I_n = I_i - I_1 + I_0 \#(6)$$

here I_n = current after standardized treatment; I_i = pulse current of any one of the 10 pulses at the rate; I_1 = first pulse current; I_0 = artificially specified current, 1 mA in positive voltage and 14 mA negative voltage. The purpose of this formula was to reset the pulse curves of all rates to the same starting point so that we can observe the current changes after ten pulses more clearly. As Δt increased, the degree of plasticity increased slowly.

$$\Delta w = \frac{G_{10} - G_1}{G_1} \text{x} 100\% \#(7)$$

where G_{10} and G_1 are the conductance values of the 10th pulse and first pulse. We obtained the curves of synaptic change weights at different Δt (**Fig. S9b**). Similar to PPF and PPD, both showed exponential changes and were greatly influenced by the positive voltage. The weight changed greatly at small Δt. The fitting curves were as follows[4]:

$$SRDP_{Potentiation} = C_5 \exp\left(-\frac{\Delta t}{\tau_5}\right) + A_3 \ \ (A_3 = 0.188, \tau_5 = 9.89) \#(8)$$

$$SRDP_{Depresstion} = C_6 \exp\left(-\frac{\Delta t}{\tau_6}\right) + A_4 \ \ (A_4 = 0.005, \tau_6 = 17.5) \#(9)$$

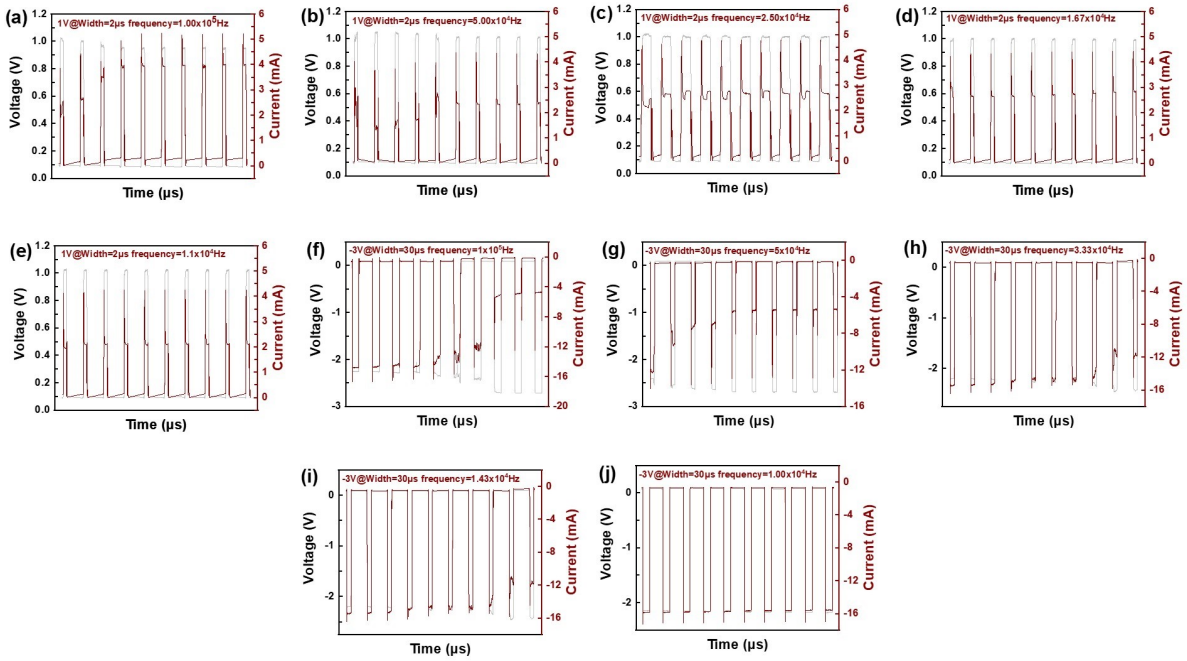

Fig. S8 Ten consecutive pulses with a positive voltage (a, b, c, d, e) (amplitude 1 V, pulse width 30 μs, Δt =10 μs, 20 μs, 40 μs, 60 μs, 100 μs); ten consecutive pulses with a negative pulse (f, g, h, i, j) (amplitude -3 V, pulse width 30 μs, Δt = 10 μs, 20 μs, 30 μs, 70 μs, 100 μs).

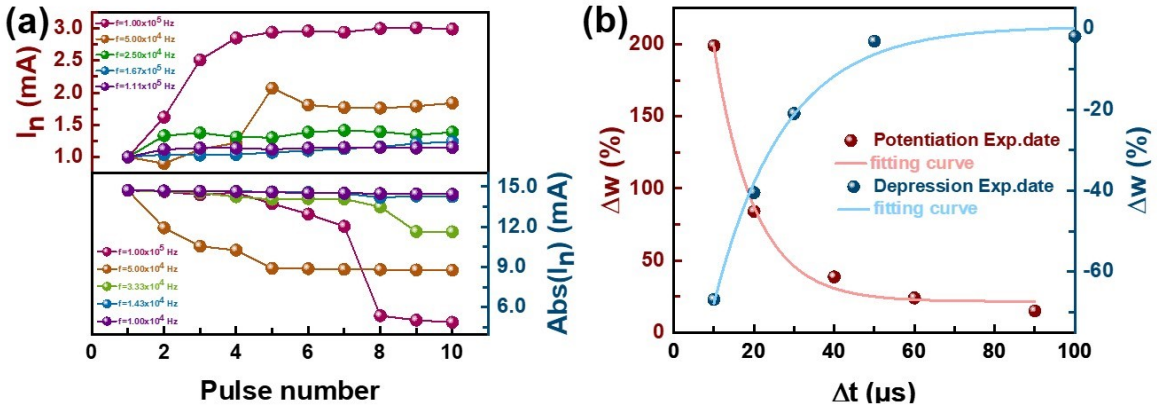

Fig. S9 (a) Current curves from ten continuous pulses with five Δt (potentiation: 10 μs, 20 μs, 40 μs, 60 μs, 90 μs; depression: 10 μs, 20 μs, 30 μs, 50 μs, 100 μs); (b) Spike rate-dependent plasticity (SRDP) with potentiation and depression process.

For biological synapses, STDP is an important function for memory and learning, so it is particularly important to simulate the STDP behavior of synapses. In STDP, synapses can adaptively adjust the connection strength between two neurons according to the learning

situation. This allows the synaptic weight to be adjusted according to Δt between the presynaptic pulse and the postsynaptic pulse. The weight calculation of its synapses was performed according to formula (7) for SRDP. However, in contrast to PPF/PPD, we defined the case of $\Delta t > 0$ and $\Delta t < 0$, respectively, when the presynaptic pulse arrived before/after the postsynaptic pulse. This led to synaptic facilitation/depression. For the case of $\Delta t > 0$, the conductance state of the device increased, but upon increasing Δt, ΔW decreased, which resulted in an exponential curve. When $\Delta t < 0$, the conductance state decreased, which shows that the synapse was in a depressed state (**Fig. S10**). The STDP experimental data were fitted by an exponential function[5]:

$$STDP_{Potentiation} = C_7 \exp\left(-\frac{\Delta t}{\tau_7}\right) + C_8 \exp\left(-\frac{\Delta t}{\tau_8}\right) + A_5 \#(10)$$

$$STDP_{Depression} = C_9 \exp\left(-\frac{\Delta t}{\tau_9}\right) + A_6 \#(11)$$

where C_7, C_8, and C_9 are scale factors, τ is the characteristic time constant of STDP, when $\Delta t > 0$, $C_7 = 5.92$, $C_8 = 0.135$, $\tau_7 = -4.36$ μs, and $\tau_9 = -54.4$ μs. Correspondingly, when $\Delta t > 0$, $C_9 = -1.59$, $\tau_9 = -10.3$ μs. The results prove that our two-terminal device successfully simulated the STDP characteristics of biological synapses by regulating Δt and order between pulses.

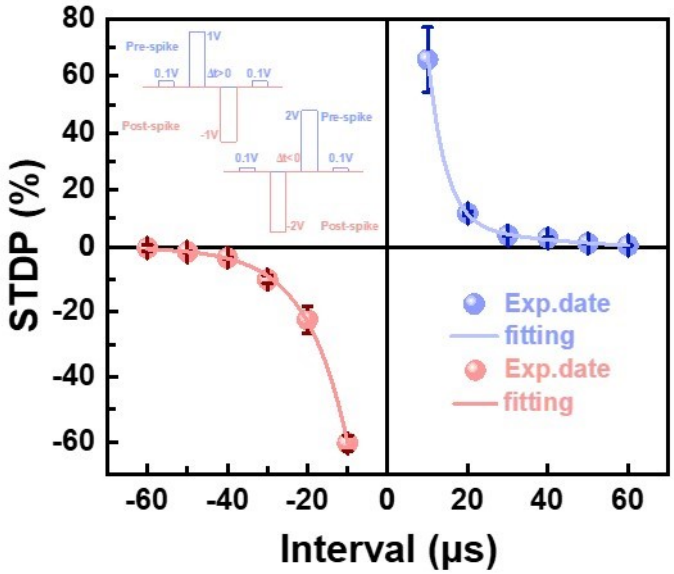

Fig. S10 Spiking-timing-dependent plasticity (STDP) in Hebbian learning rules. The input pulses of the pre-synapse and post-synapse are shown in the inset.

We also explored variations in the device conductance state under different intensity pulses, as shown in **Fig. S12a**. We utilized 15 consecutive pulses of the same width, varying only the intensity of the pulses (**Fig. S11**). The results showed that the conductance of the device decreased upon applying negative voltage pulses, but the low voltage only changed the low-conductance state, while the larger voltage changed the conductance state greatly. Formula (7) was used to calculate the weight change. After fitting with an exponential function, **Fig. 12b** was obtained[3]:

$$SVDP = C_{10}\exp\left(-\frac{\Delta t}{\tau_{10}}\right) + A_7\ (C_{10} = 0.322, \tau_{10} = 2.77\ \mu s) \#(12)$$

The results confirmed that our device successfully mimicked the properties of SVDP in biological synapses. This characteristic is very similar to a biological stress response: a large stimulus will lead to a deeper memory, which can be maintained for a long time, which is the basis of biogenesis learning and associative behavior.

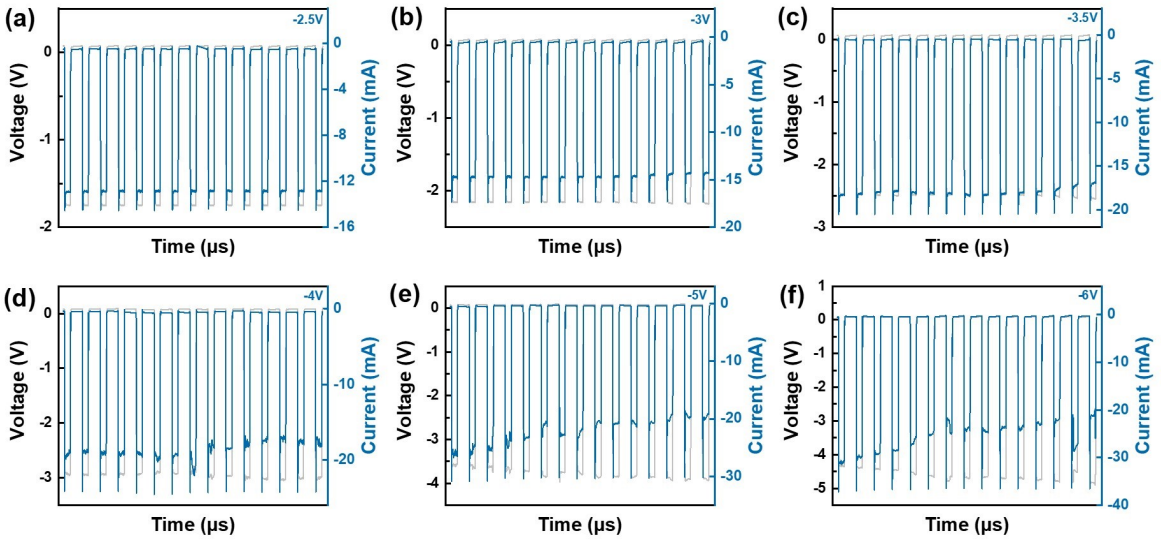

Fig. S11 15 consecutive pulses with a negative voltage (a, b, c, d, e, f) (amplitude -2.5 V, -3.0 V, -3.5 V, -4.0 V, -5.0 V, -6.0 V, respectively, pulse width = 30 μs).

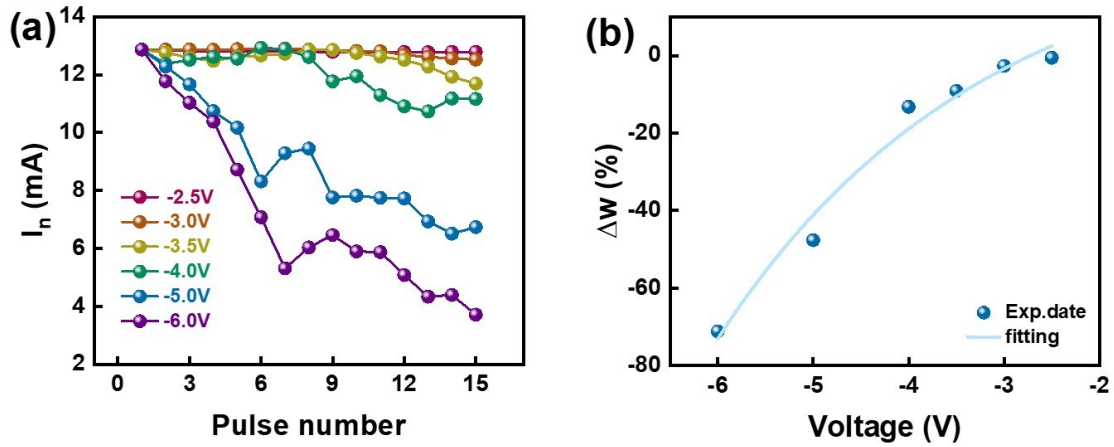

Fig. S12 (a) The current curves from 15 continuous pulses with six intensity voltage (-2.5 V, -3.0 V, -3.5 V, -4.0 V, -5.0 V, -6.0 V, original data from **Fig. S11**); (b) Spike voltage-dependent plasticity (SVDP) of device.

In addition, we simulated the biological synapse process of learning, forgetting, and relearning[1,6]. We utilized 120 positive pulses (1.8 V) to simulate the learning process. During this process, the current gradually rose, which proved that its conductance state also gradually increased. 100 negative pulses (-1.5 V) were utilized to reduce the conductance state of the device to simulate the forgetting process. During the relearning process, we only utilized 40

pulses, and the device state conductance increased to the first status. The re-forgetting process was also 100 negative pulses (-1.5 V), but the current compared to the first forgetting process significantly increased. Finally, the relearning process was completed with only 15 pulses. This corresponds to enhanced biological memory. During the process of repeated learning, forgetting, and re-learning, the connection strength between neurons increased, which means that biological memory was more permanent. It gradually changed from short-term memory to long-term memory (**Fig. S13**).

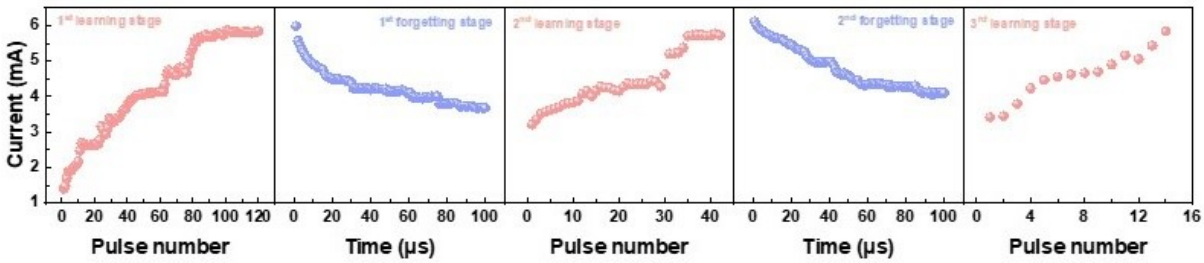

Fig. S13 Demonstration of the learning-forgetting-relearning process (learning process: amplitude 1.8 V, width 30 μs, period 90 μs, 120 pulses; forgetting process: amplitude -1.5 V, width 30 μs, period 90 μs, 100 pulses; relearning process: amplitude 1.8 V, width 30 μs, period 90 μs, 40 pulses; the second relearning process: amplitude 1.8 V, width 30 μs, period 90 μs, 15 pulses).

References

1 Q. Yan, F. Fan, C. Sun, M. E. El-Khouly, H. Liu, Y. Zheng, B. Zhang, G. Liu and Y. Chen, *J. Mater. Chem. C*, 2021, **9**, 6930–6936.

2 Y. Chen, L. R. Subramanian, M. Fujitsuka, O. Ito, S. O'Flaherty, W. J. Blau, T. Schneider, D. Dini and M. Hanack, *Chem. Eur. J.*, 2002, **8**, 4248–4254.

3 Z. Q. Wang, H. Y. Xu, X. H. Li, H. Yu, Y. C. Liu and X. J. Zhu, *Adv. Funct. Mater.*, 2012, **22**, 2759–2765.

4 Y. N. Zhong, T. Wang, X. Gao, J.-L. Xu and S.-D. Wang, *Adv. Funct. Mater.*, 2018, **28**, 1800854.

5 H. Wang, X. Yan, S. Wang and N. Lu, *ACS Appl. Mater. Interfaces*, 2021, **13**, 17844–17851.

6 X. Yan, L. Zhang, H. Chen, X. Li, J. Wang, Q. Liu, C. Lu, J. Chen, H. Wu and P. Zhou, *Adv. Funct. Mater.*, 2018, **28**, 1803728.